

Modeling and testing of COTS observation systems for night and daytime satellite detection

Ellen Glad

Millennium Space Systems, A Boeing Company

ABSTRACT

Millennium Space Systems built a mobile ground observation system using commercial off-the-shelf (COTS) components with the objective to detect and track satellites in low Earth orbit (LEO). We first demonstrated satellite tracking at night, and then we expanded this capability to daytime operations. Trades and considerations for both night and daytime observation systems are documented, focusing on our signal-to-noise (SNR) optical models to select a shortwave infrared (SWIR) sensor suitable for daytime satellite detection. We discuss our attempts to verify our models by extracting target SNR for visible and SWIR satellite detection. In general, our SNR estimates leaned conservative for our VIS observations, likely due to our model assuming a 20% reflective, spherical target. We have captured about 30 LEO satellites down to 1U CubeSat size (10cm³) and 10 geosynchronous (GEO) satellites. Our SWIR modeling results set us up for successful daytime satellite observations, allowing detection of over 10 satellites including rocket bodies and other large targets.

1. INTRODUCTION

Ground-based satellite detection has been performed for decades to support a variety of space situational awareness (SSA) activities. SSA captures the concepts of detection, tracking, and maintaining knowledge of satellites' positions over time, making it useful for applications like collision avoidance and national security. The United States Space Surveillance Network (SSN) uses several optical tracking systems globally, in addition to radar and space-based systems, to track artificial objects in Earth's orbit. Satellite detection in the visible bands relies on reflected sunlight, unless the satellite produces its own radiance. For a ground-based sensor to receive enough reflected solar signal from a satellite in low Earth orbit (LEO) lower than 2,000 kilometers in altitude above Earth, observations should optimally take place within an approximate 2-hour window before sunrise and an equivalent window after sunset, which varies depending on geographic latitude and season. This period is when the terminator, which separates day and night, passes over a given location. Geosynchronous (GEO) satellites orbit at a higher altitude of 37,500 kilometers above Earth, so depending on the season and viewing location, there is opportunity for sufficient sunlight reflection throughout the entire night.

On the contrary, when observing satellites in LEO, only a fraction of the day is usable, greatly decreasing the quantity and frequency of observable targets. The ability to observe satellites in the daytime extends opportunities for observation. Several groups have proven that the use of a shortwave infrared (SWIR) sensor is a good option for daytime satellite observations. Thomas and Cobb describe their sky spectral radiance models and validation through the detection of rocket bodies in LEO [16]. Furthermore, Numerica's Aquila system uses a SWIR small telescope system to detect satellites in GEO [15]. Fig. 1 shows the AM1.5 Global (AM1.5G) solar irradiance spectrum, which is the solar irradiance that transmits through Earth's atmosphere onto the ground. This data reflects the spectrum contained in the ASTM G-173-03 standard [12]. Fig. 1 highlights relative quantities of solar irradiance in the visible (VIS) versus the SWIR bands. The integrated irradiance over the VIS region is much higher than in the SWIR region, which is why a VIS sensor is the best option for a high signal-to-noise ratio (SNR) of a satellite across the terminator. For daytime satellite detection, it is important to determine where in the spectrum and how large a bandwidth can be tolerated to allow a higher target signal compared to the background noise.

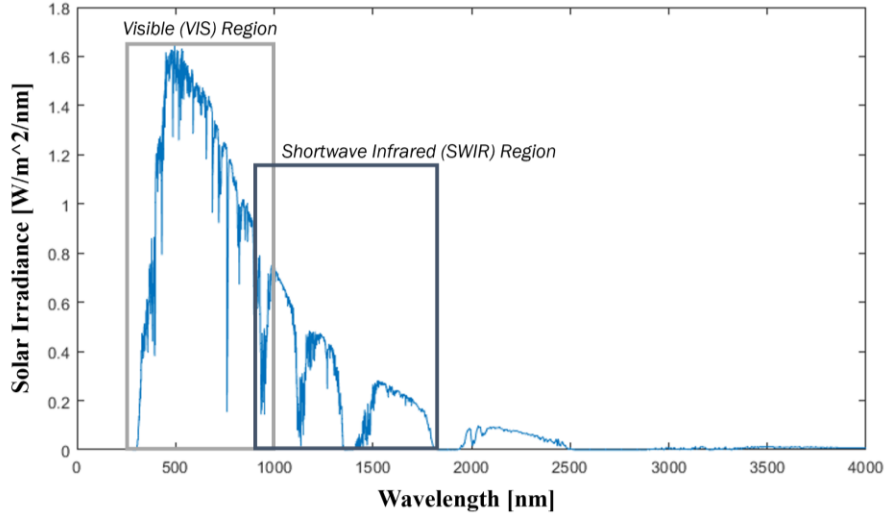


Fig. 1. AM1.5G Solar Irradiance Spectrum

2. OPTICAL MODELING AND TRADES

2.1 Visible Modeling and Trades



Fig. 2. Millennium's Satellite Detection and Tracking System

To achieve our first objective of detecting and tracking a LEO satellite during a terminator pass, we selected an optical tube assembly (OTA), visible sensor, and tracking mount. A summary of the high-level desired specifications and procured equipment is described in Table 1. Fig. 2 is a photograph of our satellite detection and tracking system with one of the two OTAs we procured. The entire system had to be mobile, i.e., portable, and able to fit in a small car for set up anywhere. To see if detection of any satellite from the ground with a mobile-sized observation system was even possible, we calculated expected visual magnitude, or apparent magnitude, mV , from example satellite targets in LEO and GEO. Eq. (1) shows the standard equation for calculating visual magnitude described by Roy and Clarke, where the Sun was used as the reference point [13]. This equation demonstrates that a decrease in 5 magnitudes is equivalent to an increase in brightness by a factor of 100.

$$mV_{Target} - mV_{Sun} = -2.5 * \log_{10}(Flux_{Target}/Flux_{Sun}) \quad (1)$$

Eq. (1) can be simplified to Eq. (2), removing terms included in both $Flux_{Target}$ and $Flux_{Sun}$. Eq. (2) uses target reflectivity a , target size r , and target range R . We calculate the phase angle factor PA_Factor from solar phase angle using the diffuse sphere phase function described by Hejduk's work on spherical satellite photometric modeling [8]. Solar phase angle describes the observer-target-sun angle, where the vertex is the target.

$$mV_{Target} - mV_{Sun} = -2.5 * \log_{10}(PA_Factor * a * (r/R^2)) \quad (2)$$

Assuming a spherical target with reflectivity a of 20% and a 90-degree solar phase angle, we calculate example satellite visual magnitudes. Fig. 3 and Fig. 4 show results for example LEO and GEO altitudes using estimates of common target sizes respectively. Using Eq. (3) described by Roy and Clarke, we estimated limiting magnitudes for varying aperture sizes, which uses the visual magnitude equation to compare a telescope's limiting magnitude to that of the human eye [13]. An optical transmission of ~65% is included in the equation which decreases visual magnitude by about half a magnitude [13]. Increasing aperture diameter D , represented in millimeters in Eq. (3), allows detection of dimmer targets.

$$mV_{Limit} = 6 + 5 * \log_{10}(D/10) \quad (3)$$

Increasing aperture also generally increases cost, along with difficulty due to set-up and take-down operations. Thus, an aperture size would be chosen to give us confidence in target detection while maintaining ease-of-use. Fig. 5 shows the visual magnitude limits for a range of aperture sizes. Based on these results, a smaller aperture towards six to eight inches would likely work for detection of most targets in both LEO and GEO, while increasing the aperture size increases likelihood for detecting dimmer targets, especially in GEO.

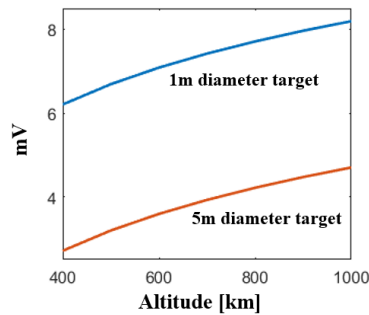


Fig. 3. Example LEO Satellite Visual Magnitudes

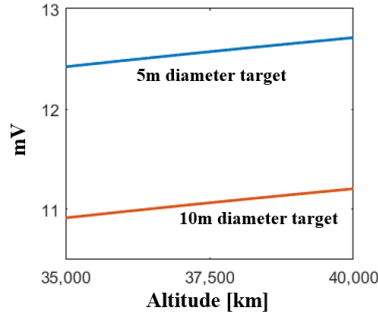


Fig. 4. Example GEO Satellite Visual Magnitudes

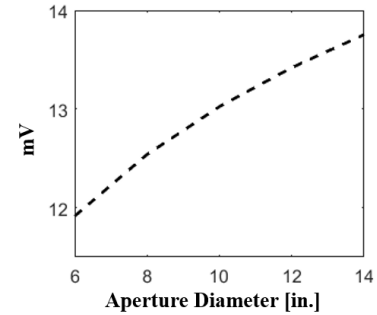


Fig. 5. Limiting Visual Magnitudes for Telescope Aperture Sizes

Besides aperture size, the other main consideration for an optical tube is focal length. Target detection is the priority over spatial resolution, so a long focal length/magnification is not a requirement. While researching previous optical systems used to detect satellites from the ground, we came across the Optical tracking and Spectral characterization for Operational Mission (OSCOM) system developed to achieve a similar goal except with a greater focus on the optical characterization of small satellites. One of OSCOM's tracking systems uses the Celestron Rowe-Ackermann Schmidt Astrograph (RASA) 11" f/2.2 OTA which has an extremely fast aperture compared to virtually all other options within the mobile-sized telescope market. Celestron also offers an 8" f/2.0 version which we considered and a 14" f/2.2 version which starts to break into the stationary-observatory realm of OTAs. The OSCOM system showed excellent results in CubeSat detection and an ability to produce precise light curves, proving a fast-aperture system is successful in dim target detection [5, 6]. We purchased the RASA 11" f/2.2 OTA which offered high light-gathering capabilities for our purposes while remaining small and simple enough to set up with 1-2 people. While waiting on the longer lead time for the RASA, we also procured the Orion 10" f/3.9 Newtonian Astrograph Reflector telescope. The Orion's design suffers from some aberrations when compared to the RASA, but nonetheless allowed for achieved CubeSat detection at an affordable price point.

Many commercial off the shelf (COTS) VIS cameras with a few main requirements will work for this application, and finding the ultimate option was not worthwhile due to the number of similarly priced, relatively cheap options. Our hard requirements included procuring a CMOS versus CCD sensor to achieve higher frame rates and a monochrome sensor versus a color sensor to increase the number of photons hitting the sensor. Other desired

characteristics included a large sensor size to ensure a larger field of view (FOV), high quantum efficiency (QE) and low noise. Because we expected to start with an open loop tracking method, a large FOV increases chances of target detection. The ZWO ASI1600MM Pro camera was selected with a 4/3" format CMOS sensor, a cooler to provide dark current <0.03 electrons per pixel per second at 0C, a read noise <4 electrons at 0 gain, 23 frames per second (FPS) frame rate at full resolution, and pixel size of 3.8 microns [3]. The camera provides a relatively large FOV of 1.64x1.24 degrees when combined with the RASA 11" OTA. Combined with the Orion OTA, the ZWO camera provides a smaller FOV of 1.0x0.77 degrees, but this is still large compared to telescope setups of similar sizes. If a second VIS camera was purchased in the future, a global shutter would be chosen (the ZWO has a rolling shutter), because a global shutter ensures that 100% of the pixels are exposed at the same time. However, it should be noted that no noticeable issues have been found due to shutter selection.

One of the biggest takeaways from this endeavor for VIS detection is that the most expensive part is the mount the optics are slewed on. We considered several tracking mounts with the following desired characteristics: 1) sufficient payload capacity to carry optical tube, sensor, and extra margin for added filters, etc., and 2) a high slew speed to maintain tracking of lower-altitude satellites in LEO. With these characteristics in mind, the Software Bisque MYT Paramount Robotic Tracking Mount was procured. Along with the tracking mount, Software Bisque offers its software, TheSkyX Professional Edition, which controls the mount and comes with several integrated tools and modules for processes including automated pointing calibrations and satellite tracking.

Table 1. VIS Observation System Desired Specifications and Hardware Procured

Component	Desired Specifications	Hardware Procured
OTA	<ul style="list-style-type: none"> • Allow detection >mV 12 for chance at GEO satellite detection <ul style="list-style-type: none"> ○ Aperture diameter >6 in. • Short focal length options to allow large FOV 	<ul style="list-style-type: none"> • Celestron RASA 11" f/2.2 OTA • Orion 10" f/3.9 Newtonian Astrograph
Camera	<ul style="list-style-type: none"> • CMOS sensor • Monochrome sensor • Large sensor size to allow large FOV • Low noise • High quantum efficiency 	ZWO ASI1600MM Pro
Mount	<ul style="list-style-type: none"> • High slew rate to allow tracking of LEO targets • Payload capacity to support selected OTA and camera with margin for filters, mounts, etc. 	Software Bisque Paramount MYT Mount

2.2 Shortwave Infrared (SWIR) Modeling and Trades

We performed a trade study on six COTS SWIR cameras with the intention to procure the lowest-risk option for daytime satellite detection. In general, the COTS SWIR camera market is small, and the options were narrowed down to the largest format arrays available, except for some higher-cost options. Table 2 lists the sensors we compared with our optical models, which ranged in cost from about \$24K to \$60K at the time of procurement.

Table 2. SWIR Sensor Options and Specifications

SWIR Camera	Spectral Range (um)	Pixel Format	Pixel Pitch (um)
Allied Vision Goldeye G-130 [7]	0.4-1.7	1280 x 1024	5
SWIR Vision Systems Acuros CQD 1920 [2]	0.4-1.7	1920 x 1080	15
SWIR Vision Systems Acuros CQD 1920 eSWIR [1]	0.35-2.0	1920 x 1080	15
NIT SenS 1280 [14]	0.9-1.7	1280 x 1024	10
Raptor Photonics Owl 1280 [11]	0.6-1.7	1280 x 1024	10
Raptor Photonics Ninnox 1280 [10]	0.6-1.7	1280 x 1024	10

Finding the lowest risk option for our application based solely on sensor parameters is not intuitive, so we built an SNR model to properly make this trade study. Our input parameters are summarized in Table 3.

Table 3. Input Parameters to SWIR SNR Model

Input Parameter	Value
Spectral Sky Radiance L_{Sky}	Estimated from data taken in Hawaii at 10:00 local time [9]
Spectral Solar Irradiance E_{Sun}	AM1.5G spectrum shown in Fig. 1 [12]
Target Size r	1-meter diameter sphere
Target Reflectivity a	20% estimated
Target Range R	600 km
Solar Phase Angle	90 degrees
Aperture Area A	Orion OTA: 0.0507 m ² (10in. diameter) RASA OTA: 0.0511 m ² (11in. diameter with 4.48" center obstruction)
Focal Length f	Orion OTA: 1000mm RASA OTA: 620mm
Optical Transmission T	90% estimated
EOD EOD	25% estimated
Pixel pitch p Quantum Efficiency QE Read Noise N_R Dark Current N_D Full Well Capacity $Full\ Well$ Frame Rate	For each camera traded, values were found through a combination of data sheets and by requests made to the manufacturers.

Our optical model is described by the following equations. First, we calculate signal due to the background sky radiance, which will be incorporated into the target SNR's noise term. Eq. (4) converts the spectral sky radiance L_{Sky} estimate into spectral sky irradiance E_{Sky} using pixel pitch p and optical focal length f . Sky radiance was estimated by using data taken at Haleakala, Hawaii at 10:00AM local time, and then we multiplied the data set by an arbitrary factor of a 10 to represent the higher uncertainty in measurement when observing from Los Angeles, California [9].

$$E_{Sky} [W/m^2/nm] = L_{Sky} * (p/f)^2 \quad (4)$$

Eq. (5) calculates sky signal S_{Sky} by integrating E_{Sky} , sensor quantum efficiency QE , and wavelength over the spectrum observed by the camera in nanometers. Additionally, aperture area A , optical transmission T , energy on detector EOD , and exposure time t in seconds are factored into this calculation.

$$S_{Sky} [pe -] = A * T * EOD * t * \int_{\lambda_1}^{\lambda_2} (E_{Sky} * QE * \lambda) d\lambda \quad (5)$$

Now, we can calculate signal due to the target. Eq. (6) calculates spectral target radiance L_{Target} in watts per steradian per square meter per nanometer using spectral solar irradiance E_{Sun} , the phase angle factor PA_Factor , which is derived from solar phase angle using the diffuse sphere phase function [8], and target reflectivity a . Eq. (7) converts target radiance into target irradiance E_{Target} using target size r and range R .

$$L_{Target} [W/Sr/m^2/nm] = E_{Sun} * PA_Factor * a \quad (6)$$

$$E_{Target} [W/m^2/nm] = L_{Target} * (r/R^2) \quad (7)$$

The signal due to the target S_{Target} is calculated similarly to S_{Sky} , except we use E_{Target} as shown in Eq. (8). All other values remain the same when modeling a given target and optical system.

$$S_{Target} [pe-] = A * T * EOD * t * \int_{\lambda_1}^{\lambda_2} (E_{Target} * QE * \lambda) d\lambda \quad (8)$$

To calculate noise N_{Target} in Eq. (9), we take the square root of the target signal with the addition of our noise sources: signal due to the sky background S_{Sky} , dark current N_D , and read noise N_R .

$$N_{Target} [pe-] = \sqrt{S_{Target} + S_{Sky} + N_D + N_R^2} \quad (9)$$

Finally, we calculate the signal to noise ratio SNR due to the target in Eq. (10):

$$SNR = S_{Target}/N_{Target} \quad (10)$$

We simulated the use of longpass filters, with cut-on wavelengths from 400-1500 nanometers, paired with the SWIR sensors to determine which portion of the band would yield the highest likelihood for target detection. One of the most interesting findings from the SWIR SNR modeling efforts was examining the time required to achieve an SNR of 10 per camera when paired with a given longpass filter. Figs. 6-7 show the required exposure times for each sensor when paired with the filters. These results are calculated with the optical parameters of the Orion OTA. The most ideal cut-on wavelength appears to be around ~800 nanometers.

However, we must analyze the exposure times when the pixel well capacity, or pixel saturation, is reached. Fig. 8 shows that time required to saturate the pixel per camera increases with higher cut-on wavelength, which makes sense because less signal is transmitting through. The calculation for exposure time of saturation is described through Eq. (11) and Eq. (12). The saturation limits resulted in large quantities of frames to be co-added for several of the sensor/filter pairings. For example, to achieve an SNR of 10, when modeled with the Orion OTA and an 800-nanometer longpass filter, we calculated over 100 frames required for the Acuros cameras, 20-40 frames required for the Owl, Ninox, and SenS cameras, and 5 frames for the Owl 1280. Therefore, the maximum frame rates for the cameras we found extended the dwell times so that it was not beneficial to use that 800-nanometer filter. The quantity of co-added frames required decreases with increased filter cut-on wavelength. And as cut-on wavelength increases, the dwell times also generally become shorter, as seen in Fig. 9.

$$Signal\ Flux_{Sum} [e-/s] = (S_{Target}/t) + (S_{Sky}/t) \quad (11)$$

$$t_{saturation} [s] = Full\ Well/Signal\ Flux_{Sum} \quad (12)$$

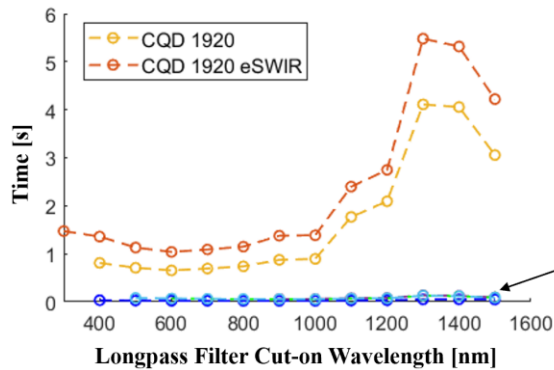


Fig. 6. Exposure Time Required to Achieve SNR=10, Modeled with Orion OTA

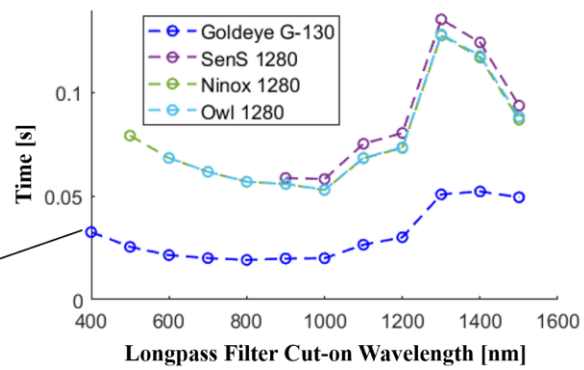


Fig. 7. Exposure Time Required to Achieve SNR=10, Modeled with Orion OTA

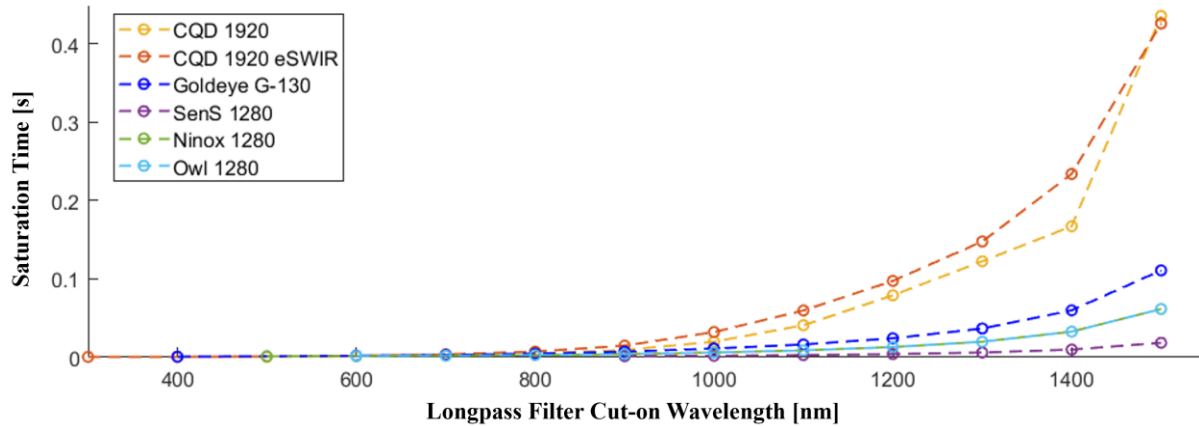


Fig. 8. Exposure Time of Pixel Saturation, Modeled with Orion OTA

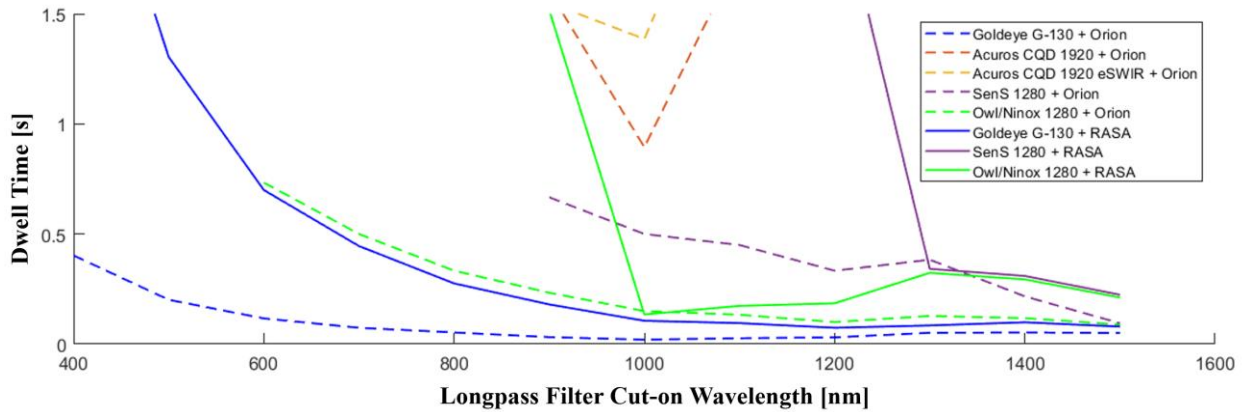


Fig. 9. Dwell Time to Achieve SNR of 10 for SWIR Sensor Options using Longpass Filters

Adding to the complexity, to assume co-adding frames is possible, the target must stay centroided on or around the same pixel when later extracting the signal from the image frame. Our open loop tracking method means that targets move from pixel to pixel across frames, so we looked through previous data sets taken of satellites in LEO with our VIS tracking system to determine an average rate of movement for a satellite target. We estimated a maximum rate of 10 arcseconds per second. Table 4 shows the amount of time a target would then take to move across a single pixel for each sensor/OTA combination.

Table 4. iFOVs for SWIR System Options

	Orion Telescope	RASA Telescope
Goldeye G-130	1.04 arcsec/pix → Target moves across pixel in 0.10s	1.69 arcsec/pix → Target moves across pixel in 0.17s
SenS/Owl/Ninox 1280	2.08 arcsec/pix → Target moves across pixel in 0.21s	3.35 arcsec/pix → Target moves across pixel in 0.34s
Acuros CQD/Acuros CQD eSWIR	3.11 arcsec/pix → Target moves across pixel in 0.33s	4.91 arcsec/pix → Target moves across pixel in 0.49s

Table 4 and Fig. 9 are compared to ensure the dwell time required for a particular sensor/OTA combination is less than the amount of time calculated for a target to move across a pixel in that configuration. The RASA's faster aperture at $f/2.2$, compared the Orion's $f/3.9$, makes it a better option for satellite detection at night because more light is collected per pixel. Focal length is shortened, which stretches the FOV, causing an increase in angular size per pixel. The RASA's aperture area is also slightly larger. While a fast aperture may be a better option at night, this may not hold true for daytime satellite detection. As shown in Fig. 9, the RASA, when combined with a few of our

sensor options, requires more dwell time to achieve the SNR threshold as when the same sensors are used with the Orion.

With plans to continue using our open-loop satellite tracking method, a large FOV was still desired. Physical sensor size and telescope focal length determine FOV. Fig. 10 shows the relative FOV sizes for our SWIR sensor options when combined with our RASA and Orion telescopes.

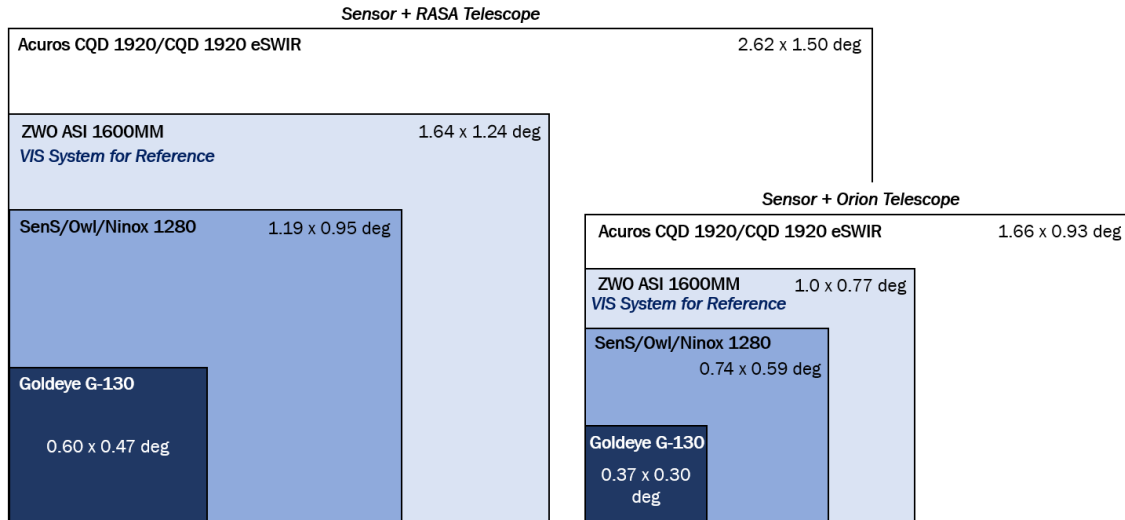


Fig. 10. Fields of View for SWIR Sensor Options with Millennium's OTAs

In addition to the factors of required dwell time and FOV, larger pixels are also helpful to keep a majority of the target signal within a single pixel. The Goldeye G-130 had great, short dwell times required to achieve the SNR threshold, but the FOV with both telescopes and the pixel size is the smallest. We procured the Raptor Photonics Owl 1280 camera and a 1500 nanometer longpass filter to balance required dwell time, FOV, and pixel size. The Owl 1280 paired with the selected filter and Orion telescope was expected to detect the modeled target within 2 co-added frames in a total dwell time of <0.09 seconds, which is shorter than the 0.21 seconds expected rate of target movement per pixel.

3. OBSERVATIONS

We conducted most of our observations in Millennium's parking lot in El Segundo, California at a latitude and longitude of 33.91697, -118.38383, at 100 feet above sea level. With our initial successful runs and frequent setup and tear down operations, it made sense to continue our observations there. However, the portability of the tracking system was beneficial when collecting observations in lower light-polluted areas.

Our standard observation sequence for satellite observations at night is described in Fig. 11, with the modifications required to observe in the daytime using the SWIR sensor. When tracking satellites at twilight hours, we can choose to do so in the morning or evening. Pointing calibrations require several frames of star fields and work much like a star tracker. The tracking mount's embedded software, TheSkyX Pro, uses an internal star catalogue to "Image Link" stars to its database. Following calibrations, a two-line element set (TLE) is inputted into the TheSkyX for each desired target which is used to estimate the satellite's position over the pass. All calibration and science images are commanded through TheSkyX as the software has built-in drivers for most common astronomy cameras.

Imaging in the daytime is not as simple. Currently, we set up the Orion telescope, mount, and VIS camera ~2 hours before sunrise and perform the necessary pointing calibrations. Then the VIS camera and cables are carefully swapped out for the SWIR equipment. There is no native driver to connect the Owl 1280 to our tracking mount, and we are actively working on software to connect the two in the future so that we can fully rely on the SWIR camera. We currently use EPIX's XCAP software to collect images with the Owl 1280. Another challenge is the additional equipment necessary. The camera link cables from the frame grabber are constrained at 2 meters length, so we constructed a mount to secure the frame grabber onto the telescope. We kept the frame grabber secured on the

telescope from the beginning of setup so that the weight is accounted for when the telescope is balanced using its counterweights.

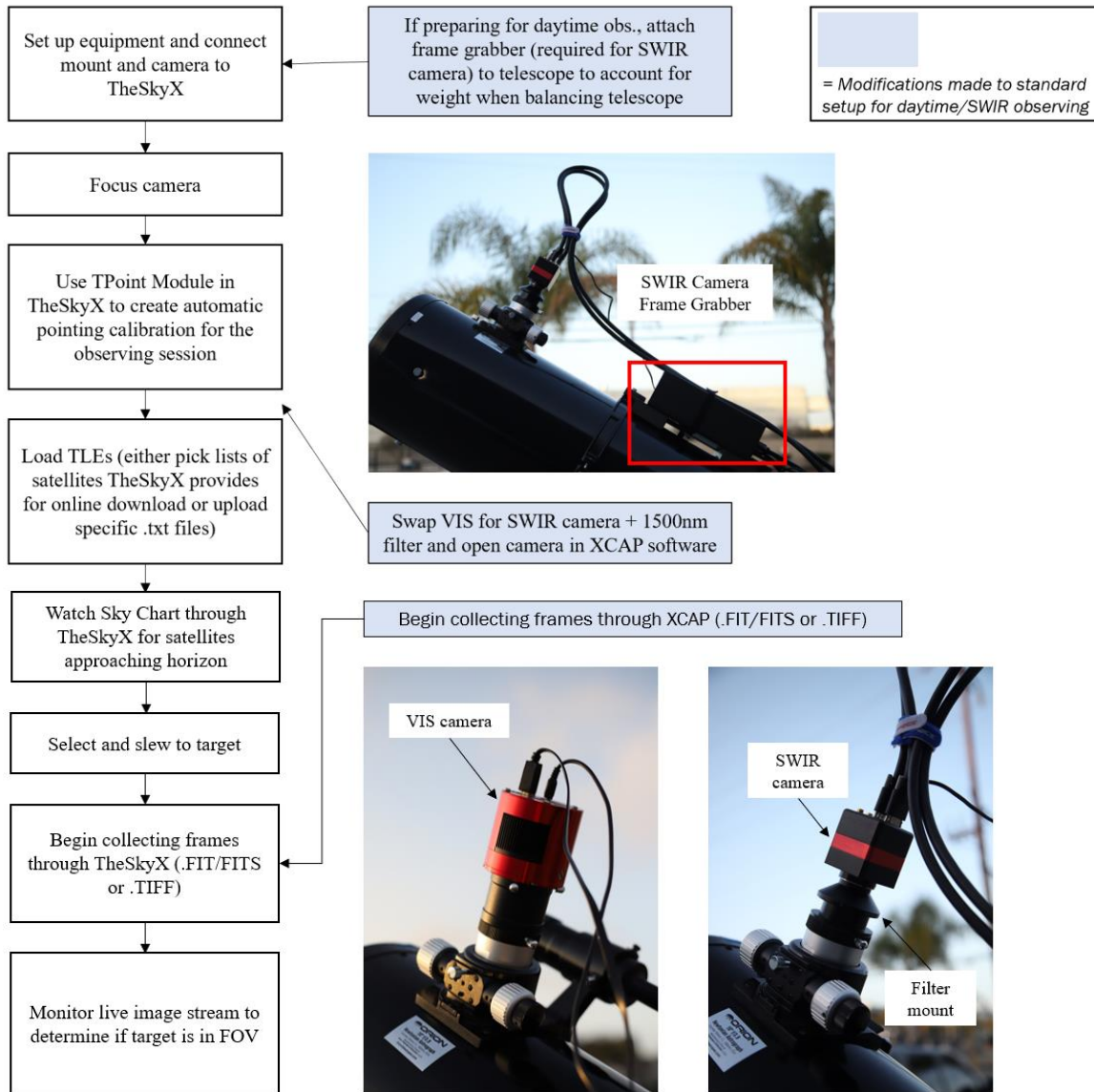


Fig. 11. Observation Sequence for Satellite Detection

With the VIS tracking systems, we detected almost 30 satellites in LEO and over 10 satellites in GEO, with an even split between using the two OTAs. We detected over 10 satellites using the SWIR setup in the morning up to three hours after sunrise. Fig. 12 displays examples of individual image frames from our VIS and SWIR setups. As we anticipated, most satellites we detected were too small to obtain any spatial resolution. However, the ISS's angular size was large enough compared to our VIS system's image scale that we could resolve the spacecraft from its solar panels as it transited across the Sun (Fig. 13). This along with other location-specific celestial events is another reason it is beneficial to own a mobile system.



Fig. 12. Example Image Frames using Millennium's VIS (left) and SWIR (right) Tracking Systems

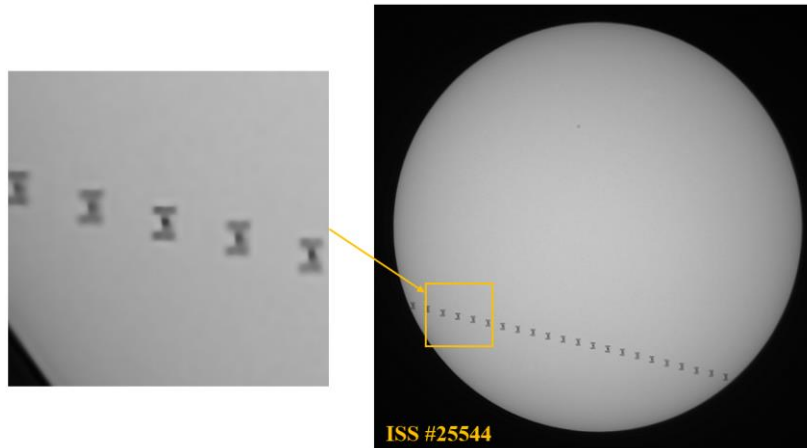


Fig. 13. Composite of Resolved Images of ISS Solar Transit using Millennium's VIS Tracking System

4. RESULTS

Using the software AstroImageJ, we extracted SNR measurements over time for successful observations, producing a version of a “light curve.” We excluded detection data with saturated target pixels or with too few frames. In Figs. 14-20, each data point in “Measured SNR,” marked with a blue dot, represents the target’s SNR from a single image frame. Aperture photometry within AstroImageJ computes centroid location per image frame, and then multiple automatically computed parameters are stored into a table for analysis including background-subtracted target signal, sky signal, and SNR. SNR is calculated from dividing the background-subtracted target signal by noise. Eq. (13) shows AstroImageJ’s calculation of noise, which relies on user-inputted dark current FD , read noise FR , and camera gain conversion G [4]. We used the manufacturer specifications for read noise and dark current at the sensor temperatures that observations were collected at, which were 0C and +15C for the ZWO and Owl 1280, respectively. Because our modeled calculations for noise do not currently account for system gain, we use a value of 1.0 for G .

$$N = \frac{\sqrt{GF_* + n_{pix}(1 + \frac{n_{pix}}{n_b})(GF_S + F_D + F_R^2 + G^2\sigma_f^2)}}{G} \quad (13)$$

4.1 Visible Observations Results

We present examples from our VIS tracking results for two satellites in LEO and one in GEO, shown in Figs. 14-16. Because we collected visible image data through TheSkyX software, a list of parameters is automatically saved per image file in the file headers. We collected VIS images in the Flexible Image Transport System (FITS) raw file type. An Angles-only Initial Orbit Determination method was used to get an estimate of the orbital state to calculate solar phase angle, using the recorded azimuth and elevation (Az/EI) angles, or right ascension and declination (RA/Dec) coordinates, in addition to the date and time recorded per image. We also used the recorded elevation angles per image to calculate the slant range to the target over time, because the listed orbital altitude found online for a given target only applies at zenith (a 90-degree elevation angle). We listed all the input parameters and their sources in Table 5 and color-coded them by our confidence levels in the inputs' accuracies when compared to more realistic/ "truth" inputs. This data shows areas in which we can try to improve our models in the future.

Table 5. Inputs to Modeled SNR for VIS Targets and their Accuracy Ratings

Parameter	Value inputted for <i>Modeled SNR</i> and confidence level in accuracy		
	High confidence	Medium confidence	Low confidence
Solar Irradiance	Data from ASTM G173-03 for AM1.5G spectrum		
Target Range	Calculated per image frame using elevation angles recorded in FITS headers		
Target Solar Phase Angle	Calculated per image frame using RA/Dec and Az/EI angles recorded in FITS headers		
Target Size and Orientation	Estimated size from online sources per target; modeled as a sphere		
Target Reflectivity	Assumed $\alpha=20\%$		
Aperture Diameter	Data from manufacturer (D_RASA=11 in., D_Orion=10 in.)		
Optical Transmission	Assumed $T=90\%$		
Sensor QE	Data from manufacturer (precise to nanometer-scale)		
Exposure Time	Recorded in FITS headers		
Dark Current	Data from manufacturer ~ 0.03 e-/p/s @ 0C		
Read Noise	Data from manufacturer ~ 3.6 e-		

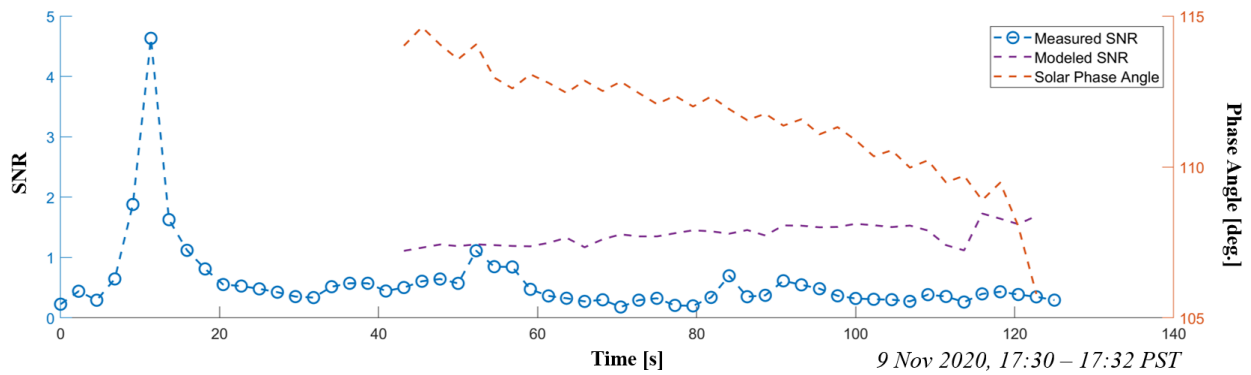


Fig. 14. CUBESAT XI-IV # 27848 SNR vs Time

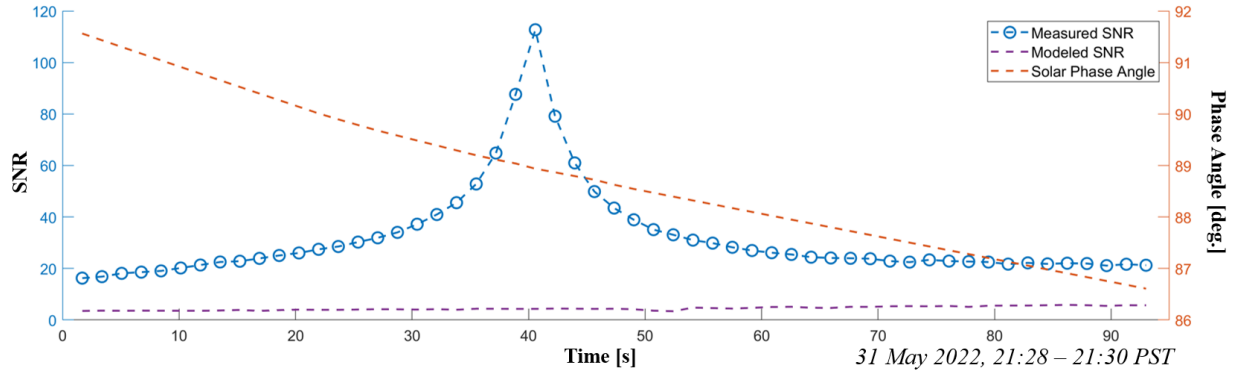


Fig. 15. HORYU-4 #41340 SNR vs Time

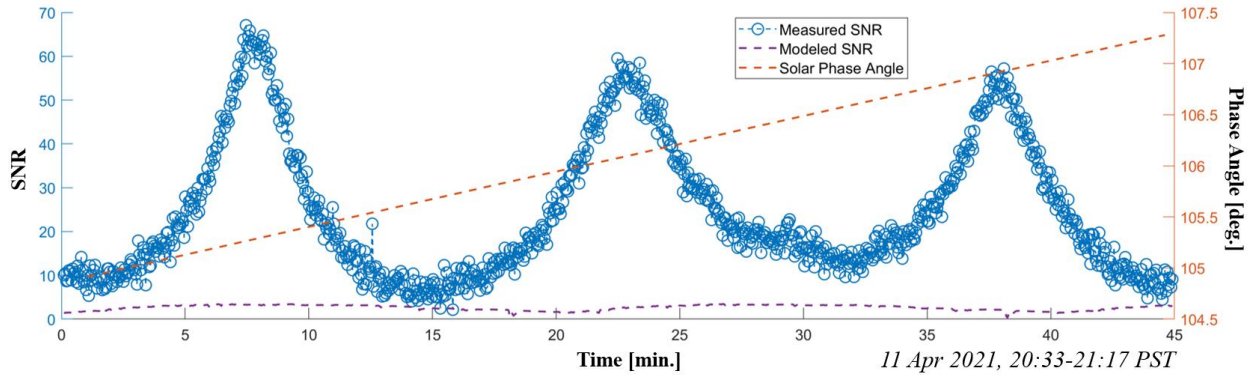


Fig. 16. GOES-15 #36411 SNR vs Time

4.2 SWIR Observations Results

We successfully detected and tracked over ten targets in LEO. All targets were large, with our current list including seven rocket bodies, five large satellites, and the ISS. Several CubeSats have been attempted with no luck yet. In the future, planning out CubeSat targets with a smaller solar phase angle and high peak elevation angle should allow chance of detection. Table 6 includes the list of inputs used to calculate Modeled SNR shown in Figs. 17-20 along with our confidence ratings for each input's accuracy to "ideal" inputs to make the model outputs realistic. Compared to the VIS inputs, a larger fraction of SWIR modeling inputs is ranked low-confidence due to the position of the telescope's pointing not being recorded per image. Also in work is a method to measure sky radiance for every observing session. Still, we used estimates of the respective target's size, spectral data from the AM1.5G spectrum, and characteristics about our optical system to show modeled comparisons to the measured data. Two cases were calculated for Modeled SNR: a 30-degree elevation angle and a 60-degree elevation angle, both at a 90-degree solar phase angle.

Table 6. Inputs to Modeled SNR for SWIR Targets and their Accuracy Ratings

Parameter	Value inputted for <i>Modeled SNR</i> and confidence level in accuracy		
	High confidence	Medium confidence	Low confidence
Solar Irradiance	Data from ASTM G173-03 for AM1.5G spectrum		
Sky Radiance	Estimated from previous published papers [9]		
Target Range	No position information recorded. Estimates calculated based on target ranges at zenith and at 1) 30 deg. elevation 2) 60 deg. elevation		
Target Solar Phase Angle	No position information recorded. Estimate of 90 deg. angle used.		
Target Size	Estimated from online sources per target (modeled as a sphere)		
Target Reflectivity	Assumed $a=20\%$		
Aperture Diameter	Data from manufacturer $D=10$ in.		
Focal Length	Data from manufacturer $f=1000$ mm		
Optical Transmission	Assumed $T=90\%$		
Sensor QE	Data from manufacturer (precise to nanometer-scale)		

Exposure Time	Recorded manually (varied per collect from 40-60ms)
Full Well Capacity	Data from manufacturer 450ke
Dark Current	Data from manufacturer ~19ke-/p/s @ 15C
Read Noise	Data from manufacturer ~180e-

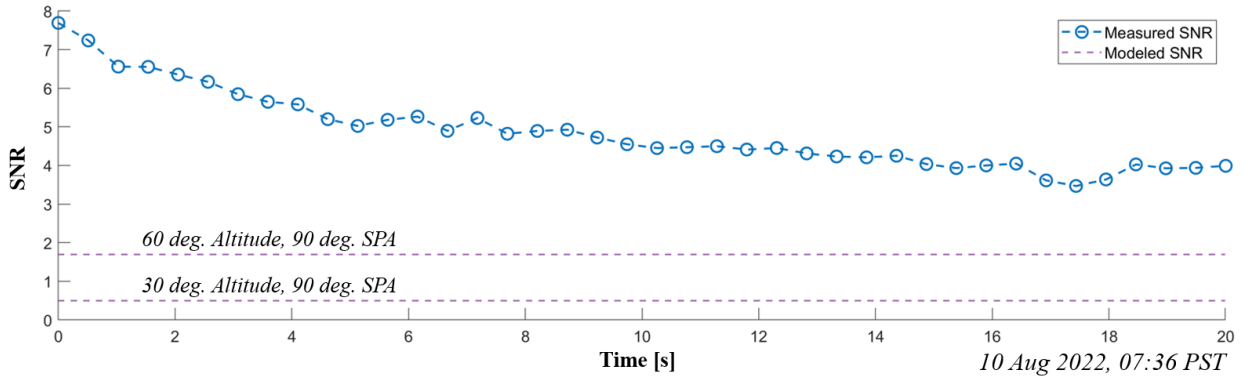


Fig. 17. OAO 2 #3597 SNR vs Time

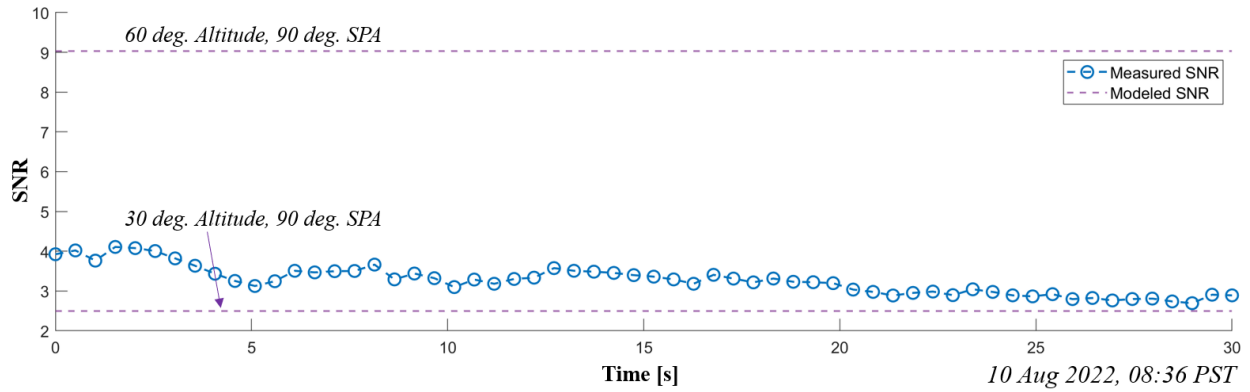


Fig. 18. COSMOS-2151 #21422 SNR vs Time

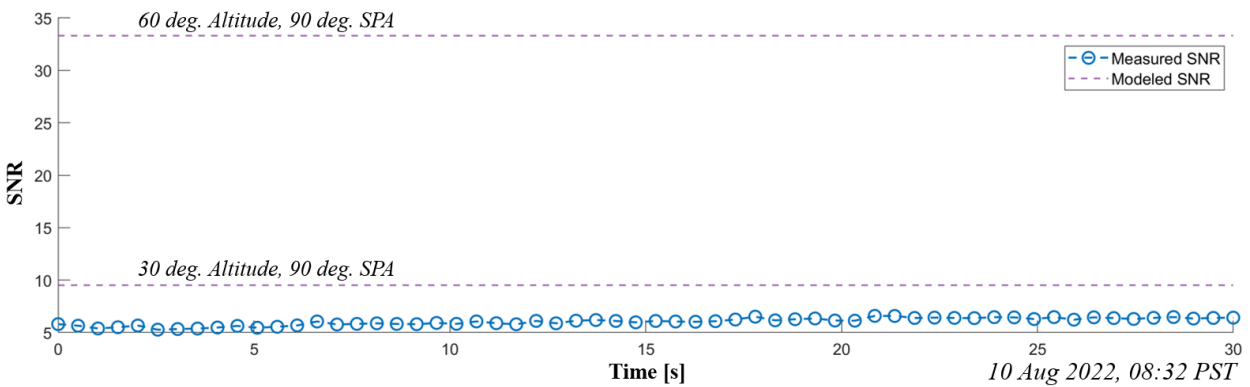


Fig. 19. SL-16 R/B #22220 SNR vs Time

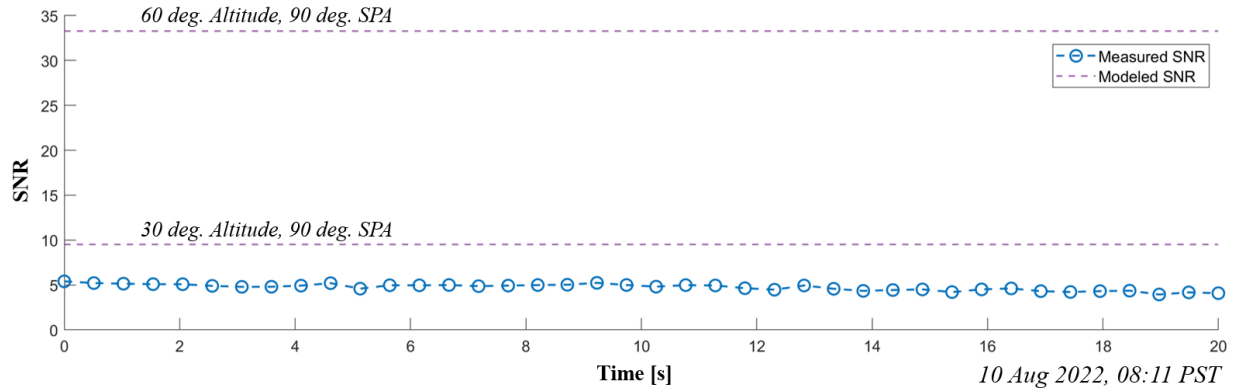


Fig. 20. SL-16 R/B #23705 SNR vs Time

In addition to the satellite detection observations made with our SWIR system, we also observed known stars for further model validation. Observations of the star Mirach were made with both a 1300-nanometer longpass and a 1500-nanometer longpass filter, at three different exposure times: 20, 40, and 92 milliseconds. Like the satellite detections, SNR for the star was extracted using AstroImageJ, and the average SNR over 10 frames was used to calculate Measured SNR shown below for each data point [4]. Now, the modeled SNR for a star is simpler to compute than for a satellite, because we model its blackbody radiation from the star’s temperature, and then we use size and range estimates to obtain star irradiance. Fig. 21 shows our measured and modeled SNR values for exposure time and filter combinations. The results showed a limiting exposure time of two milliseconds using the 1300 nanometer filter and six milliseconds using the 1500 nanometer filter. Clearly, the test data showed a longer exposure time was allowed, but the pixels did begin to saturate around the 40-millisecond mark for both filters. The SWIR satellite detection modeling showed a 1500 nanometer filter would result in a higher SNR in a shorter amount of time compared to the use of a shorter cut-on wavelength, so an additional motive for running this test was to compare these two filters. The number of data points is small, but the 1500-nanometer showed a higher SNR at the longest exposure time, resembling the modeled results.

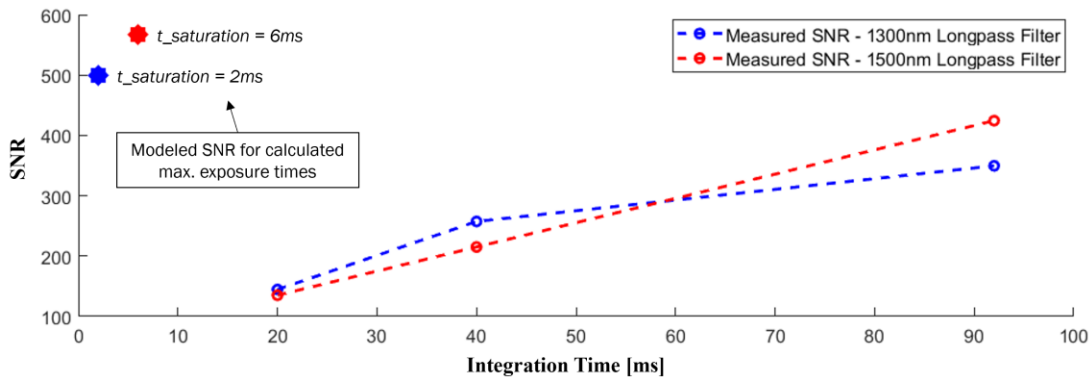


Fig. 21. Measured vs Modeled SNR for Mirach

5. CONCLUSIONS

Our testing clearly demonstrated the ability of COTS components to detect satellites from the ground in the daytime. Our SNR modeling results for daytime satellite detection are more challenging to verify currently due to the lack of pointing data per collected image frame. One of the more immediate future tasks is to complete software development to allow automatic recording of Az/EI angles or RA/Dec coordinates per image. Other future work may include detecting CubeSats in LEO or satellites in GEO and co-adding frames to extract signal. A closed-loop tracking system also would be beneficial to increase the amount of data per satellite pass since the target would remain in the FOV longer. Now that we have optical models and a first pass at model verification, we can try to update our models, e.g., measuring sky radiance at our observing site, to improve our estimates. The ability to model optical systems, collect observation data from satellites, and validate models is a useful tool to be more knowledgeable when considering optical systems for SSA applications.

6. ACKNOWLEDGMENTS

Thank you to Henry Chong for building support equipment to make daytime observations possible, and to both Henry and Nicholas-Tyler Howard for every early morning and late night you both have spent helping to collect observation data. Thank you to Tom Chrien and Ryan Lawrence for your encouragement and mentorship throughout this research. Thank you to James Johnson for providing tools and analysis from an astrodynamics perspective for creating the results presented in this paper.

7. REFERENCES

- [1] Acuros CQD 1920 GigE eSWIR Camera, SWIR Vision Systems, https://www.swirvisionsystems.com/wp-content/uploads/Acuros-1920-GigE-002-Camera_2022-1.pdf.
- [2] Acuros CQD 1920 GigE SWIR Camera, SWIR Vision Systems, https://www.swirvisionsystems.com/wp-content/uploads/Acuros-1920-GigE-001-Camera_2022-1.pdf.
- [3] ASI1600MM Pro (mono), ZWO, <https://astronomy-imaging-camera.com/product/asi1600mm-cool>.
- [4] K. A. Collins, J. F. Kielkopf, K. G. Stassun, F. V. Hessman. AstroImageJ: Image Processing and Photometric Extraction for Ultra-Precise Astronomical Light Curves (Expanded Edition), arXiv:1701.04817 [Astro-ph.IM], 2017, <https://arxiv.org/pdf/1701.04817.pdf>.
- [5] F. Gasdia. Optical Tracking and Spectral Characterization of Cubesats for Operational Missions, *Dissertations and Theses, 212*, 2016, <https://commons.erau.edu/edt/212/>.
- [6] F. Gasdia, A. Barjatya, S. Bilardi. Multi-Site Simultaneous Time-Resolved Photometry with a Low Cost Electro-Optics System, *Sensors*, Multidisciplinary Digital Publishing Institute, 2017, <https://www.ncbi.nlm.nih.gov/pmc/articles/PMC5492105/>.
- [7] Goldeye G-130 TEC1, Allied Vision, <https://www.alliedvision.com/en/camera-selector/detail/goldeye/g-130-tec1/>.
- [8] M. D. Hejduk. Specular and Diffuse Components in Spherical Satellite Photometric Modeling, *Advanced Maui Optical and Space Surveillance Technologies Conference*, Maui, Hawaii, 2011, <https://amostech.com/TechnicalPapers/2011/NROC/HEJDUK.pdf>.
- [9] K. T.C. Jim, B. N. Gibson, E. A. Pier. Daytime Sky Brightness Modeling of Haleakala along the GEO Belt, *Advanced Maui Optical and Space Surveillance Technologies Conference*, Maui, Hawaii, 2012, <https://amostech.com/TechnicalPapers/2012/POSTER/JIM.pdf>.
- [10] Ninox 1280, Raptor Photonics, <https://www.raptorphotonics.com/wp-content/uploads/2022/03/Ninox-1280-US-Letter.pdf>.
- [11] Owl 1280, Raptor Photonics, <https://www.raptorphotonics.com/wp-content/uploads/2022/03/OWL-1280-US-Letter.pdf>.
- [12] Reference Air Mass 1.5 Spectra. National Renewable Energy Laboratory. <https://www.nrel.gov/grid/solar-resource/spectra-am1.5.html>.
- [13] A. E. Roy, D. Clarke. *Astronomy: Principles and Practice, 4th Edition*, https://www.academia.edu/41720617/Astronomy_Principles_and_Practice_Roy_and_Clarke.
- [14] SenS 1280, New Imaging Technologies, <https://new-imaging-technologies.com/product/sens-1280/>.
- [15] J. Shaddix, J. Brannum, A. Ferris, A. Hariri, A. Larson, T. Mancini, J. Aristoff. Daytime GEO Tracking with ‘Aquila’: approach and results from a new ground-based SWIR small telescope system. *Advanced Maui Optical and Space Surveillance Technologies Conference*, Maui, Hawaii, 2019, https://s11967.pcdn.co/wp-content/uploads/2019/11/Numerica_AQUILA_AMOS2019.pdf.
- [16] G. M. Thomas, R. G. Cobb. Ground-based, daytime modeling and observations in SWIR for satellite custody. *Advanced Maui Optical and Space Surveillance Technologies Conference*, Maui, Hawaii, 2019, <https://amostech.com/TechnicalPapers/2019/Optical-Systems-&-Instrumentation/Thomas.pdf>.